Spectral shift of solid high-order harmonics from different channels in a combined laser field

Dong-Dong Cao(曹冬冬)[1], Xue-Fei Pan(潘雪飞)[2], Jun Zhang(张军)[1,†], and Xue-Shen Liu(刘学深)[1,‡]

[1] *Institute of Atomic and Molecular Physics, Jilin University, Changchun* 130012, *China*
[2] *College of Science, Northeast Forestry University, Harbin* 150040, *China*

(Received 6 September 2022; revised manuscript received 9 November 2022; accepted manuscript online 22 November 2022)

We investigate theoretically the spectral shift of the high-order harmonic generation (HHG) in ZnO driven by a combined laser field by solving the two-band semiconductor Bloch equations (SBEs) in the velocity gauge. The combined laser field is synthesized by a fundamental laser pulse and its seventh-frequency laser pulse. When the seventh-frequency laser pulse is added to the rising or falling parts of the fundamental laser field, we find that the spectral blueshift or redshift appears, which is due to the unequal contribution of the rising and falling parts in the fundamental laser field to the harmonics. By analyzing the time-dependent conduction band population in $\boldsymbol{k}$ space, we found that, in addition to the tunneling ionization channel, there is also the resonant electron injection channels which is induced by the seventh-frequency laser pulse. The harmonics generated by the different channels show the spectral redshift or the spectral blueshift, respectively. Through analyzing the $\boldsymbol{k}$-integrated transient conduction band population of the electrons from different channels, we found that if there is a certain delay in the process of the electron excitation, it will lead to the delay in the harmonic emission, which results in the spectral redshift of the harmonics.

Keywords: high-order harmonic generation, ZnO crystal, spectral shift of harmonics, resonant electron injection channels

PACS: 32.80.Rm, 42.65.Ky, 42.65.Re **DOI:** 10.1088/1674-1056/aca4bf

1. Introduction

The interaction between intense laser pulse and gases has revealed a series of high-order nonlinear optical phenomena in the past several decades.[1,2] High-order harmonic generation (HHG)[3] is a significant tool to generate coherent extreme ultraviolet (EUV) attosecond pulses[4–7] and can be used to trace the ultrafast electronic dynamics of atomic or molecular targets.[8–10] The HHG can also be used to realize the imaging of molecular orbitals and structures.[11] In recent years, the HHG of the solid has attracted much attention both experimentally[12] and theoretically.[13,14] The solid HHG with low driving laser intensity and high emission efficiency offers a new way to obtain efficient and compact attosecond light sources. The solid HHG creates a new opportunity for the investigation of the detection of attosecond electron dynamics in the bulk crystal.[15,16]

In order to understand the microscopic processes of electronic motion in bulk crystal, some physical models and theoretical methods have been developed, such as semiconductor Bloch equations (SBEs),[14–17] the time-dependent Schrödinger equation (TDSE),[18,19] and the time-dependent density-functional theory.[20,21] There are two physical processes of the solid HHG: the intraband and the interband process. A three-step model in crystal momentum space can be used to explain the interband processes of the solid HHG.[14] The electron tunnels from the valence band to the conduction band so that an electron–hole pair is formed; the electron (hole) in the conduction (valence) band is accelerated by the laser field, resulting in the intraband current; the electron recombines with the hole and emits a high-energy photon with an energy given by the energy difference between the conduction and valence band states at the final momentum.

Many significant works have contributed to the research of the spectral shift of the harmonics. For example, Du *et al.*[22] investigated the spectral redshift of the He^+ when a VUV laser pulse was added to the falling part of the fundamental field. Through the time-frequency analysis, it is indicated that the spectral redshift can be observed when a weak VUV pulse is added in the falling part of the fundamental pulse. The relationship between the harmonic instantaneous frequency and the laser field intensity is given by $\omega_q(t) = q\omega + \alpha_q[\partial I(t)/\partial t]$,[23,24] where ω_0 is the frequency of the laser field, q is the harmonic order. In the rising part of the laser field, the amplitude of continuous laser cycles is larger than that of the previous laser cycle, $\partial I(t)/\partial t > 0$. Thus the harmonic order gets large and spectral blueshift will be observed. In the falling part of the laser pulse, the amplitude of the continuous laser cycles is small than that of the previous laser cycle, $\partial I(t)/\partial t < 0$, and the spectral redshift will appears. Many researchers have explored the spectral shift of atoms and molecules both experimentally[25,26] and theoretically[27,28] in the past several decades. The phe-

†Corresponding author. E-mail: junzhang@jlu.edu.cn
‡Corresponding author. E-mail: liuxs@jlu.edu.cn

© 2023 Chinese Physical Society and IOP Publishing Ltd

nomenon of the spectral redshift in the solid HHG is also observed, and the redshift appears on the higher plateau, which can be explained by the step-by-step model.[24,29]

In this paper, we investigate theoretically the spectral shift of the solid high-order harmonics in a combined laser field, which is synthesized by a fundamental laser pulse and its seventh-frequency laser pulse. By time-frequency analysis, we found that the spectral shift is due to the unequal contribution of the rising and falling parts of the laser field to the harmonics. By analyzing the time-dependent population of the conduction band in the $\boldsymbol{k}$ space, it is found that the tunneling ionization channel and the resonant electron injection channels which is induced by the seventh-frequency laser pulse are contributed to the solid HHG. Through the crystal momentum-resolved profiles of the harmonics,[17,30] we found that the spectral blueshift or redshift of the harmonics produced by electrons from different channels in $\boldsymbol{k}$ space can be observed, which is due to the inconsistent excitation moments of the electrons from different channels.

2. Theoretical method

We investigate the solid HHG by solving the two-band semiconductor Bloch equations (SBEs) in the velocity gauge[14,15] (Atomic units are used throughout the paper)

$$\dot{\pi}(\boldsymbol{K},t) = -\frac{\pi(\boldsymbol{K},t)}{T_2} - \mathrm{i}\Omega(\boldsymbol{K},t)\omega(\boldsymbol{K},t)\,\mathrm{e}^{-\mathrm{i}S(\boldsymbol{K},t)}, \quad (1)$$

$$\dot{n}_m(\boldsymbol{K},t) = \mathrm{i}s_m\Omega^*(\boldsymbol{K},t)\pi(\boldsymbol{K},t)\,\mathrm{e}^{\mathrm{i}S(\boldsymbol{K},t)} + \mathrm{c.c.}, \quad (2)$$

where $\pi(\boldsymbol{K},t)$ is the polarization strength between the conduction band (CB) and the valence band (VB), n_m is the population of the VB ($m=\mathrm{v}$, $s_m=-1$) and the CB ($m=\mathrm{c}$, $s_m=1$). $\omega(\boldsymbol{K},t) = n_\mathrm{v}(\boldsymbol{K},t) - n_\mathrm{c}(\boldsymbol{K},t)$ is the population difference. T_2 is the dephasing time. $\Omega(\boldsymbol{K},t) = \boldsymbol{E}(t)\cdot d[\boldsymbol{K}+\boldsymbol{A}(t)]$ is the Rabi frequency, and where $d[\boldsymbol{K}+\boldsymbol{A}(t)]$ is the transition dipole moment (TDM) between the VB and the CB, $\boldsymbol{A}(t) = -\int \boldsymbol{E}(t)\mathrm{d}t$ is the laser vector potential, $\boldsymbol{E}(t)$ is the electric field of the laser. According to the Bloch acceleration theorem,[31] the initial crystal momentum $\boldsymbol{k}$ can be transformed into a moving frame $\boldsymbol{K}(t)$ by $\boldsymbol{K}(t) = \boldsymbol{k} - \boldsymbol{A}(t)$, and the first Brillouin zone (BZ) can be shifted to $\overline{\mathrm{BZ}} = \mathrm{BZ} - \boldsymbol{A}(t)$.[14] $S(\boldsymbol{K},t) = \int_{-\infty}^{t} \varepsilon_\mathrm{g}[\boldsymbol{K}+\boldsymbol{A}(t')]\,\mathrm{d}t'$ is the classical action and $\varepsilon_\mathrm{g} = E_\mathrm{c} - E_\mathrm{v}$ is the band gap between the VB and the CB, where E_c and E_v are the energy values of the VB and the CB, respectively.

The intraband current and interband current can be obtained by

$$\boldsymbol{j}_\mathrm{ra}(t) = \sum_{m=\mathrm{c,v}} \int_{\overline{\mathrm{BZ}}} \boldsymbol{v}_m[\boldsymbol{K}+\boldsymbol{A}(t)] n_m(\boldsymbol{K},t)\,\mathrm{d}^3\boldsymbol{K}, \quad (3)$$

$$\boldsymbol{j}_\mathrm{er}(t) = \frac{\mathrm{d}}{\mathrm{d}t}\int_{\overline{\mathrm{BZ}}} \boldsymbol{p}(\boldsymbol{K},t)\,\mathrm{d}^3\boldsymbol{K}, \quad (4)$$

where $\boldsymbol{v}_m(\boldsymbol{k}) = \nabla_{\boldsymbol{k}} E_m(\boldsymbol{k})$ denotes the band velocity in the VB ($m=\mathrm{v}$) or in the CB ($m=\mathrm{c}$), and $E_m(\boldsymbol{k})$ is the band dispersion. $\boldsymbol{p}(\boldsymbol{K},t) = d[\boldsymbol{K}+\boldsymbol{A}(t)]\pi(\boldsymbol{K},t)\,\mathrm{e}^{\mathrm{i}S(\boldsymbol{K},t)} + \mathrm{c.c.}$ is the polarization of the two bands related with $\pi(\boldsymbol{K},t)$.[14] The intraband and interband high-order harmonics can be obtained from the Fourier transform (FT) of $\boldsymbol{j}_\mathrm{ra}(t)$ and $\boldsymbol{j}_\mathrm{er}(t)$, respectively. The total current driven by the laser field is: $\boldsymbol{j}(t) = \boldsymbol{j}_\mathrm{ra}(t) + \boldsymbol{j}_\mathrm{er}(t)$. Then the solid high-order harmonic spectrum can be obtained by the modulus square of Fourier transform of the total current:

$$I(\omega) = \omega^2 |FT\{\boldsymbol{j}(t)\}|^2. \quad (5)$$

In this paper, we investigate the HHG of the ZnO crystal under linearly polarized combined laser field. The combined laser field consists of a driving pulse and its seventh-frequency laser pulse. The seventh-frequency laser pulse is used to excite the electrons from the VB to the CB. The polarization direction of the laser is along the Γ–M direction of the ZnO crystal. The parameters of the band dispersion relation of the ZnO crystal are taken from Ref. [15]. The crystal-momentum-dependent transition dipole moments are calculated by Eq. (7) in Ref. [32]. The combined laser field is given by

$$\boldsymbol{E}(t) = f_0(t)\boldsymbol{E}_0\cos(\omega_0 t) + f_1(t)\boldsymbol{E}_1\cos(\omega_1(t-t_\mathrm{delay})), \quad (6)$$

where

$$f_0(t) = \exp[-2\ln(2)t^2/\tau_0^2],$$
$$f_1(t) = \exp[-2\ln(2)(t-t_\mathrm{delay})^2/\tau_1^2]$$

are Gaussian-type envelope, $\tau_0 = 40$ fs and $\tau_1 = 15$ fs are the full width at half maximum (FWHM) of the fundamental pulse and the seventh-frequency laser pulse, respectively. t_delay is the time delay of the two laser pulses. $\boldsymbol{E}_0 = 0.004$ a.u., $\boldsymbol{E}_1 = 0.0015$ a.u. are the amplitudes of the laser pulse, $\omega_0 = 0.01732$ a.u. is the fundamental frequency, the wavelength $\lambda = 2629$ nm, and the dephasing time is chosen as $T_2 = 2.725$ fs.

3. Results and discussion

In our investigation, a 2629-nm laser pulse is used as the driving laser pulse and its seventh-frequency laser pulse (376 nm) is added to the fundamental laser pulse to enhance the harmonic emission effciency. Figures 1(a)–1(c) show the electric fields for time delay $t_\mathrm{delay} = -2$ o.c. (o.c. is short for optical cycle), $t_\mathrm{delay} = 0$, and $t_\mathrm{delay} = 2$ o.c., where the solid black lines display the fundamental laser field and its seventh-frequency laser pulses with time delay $t_\mathrm{delay} = -2$ o.c., $t_\mathrm{delay} = 0$, $t_\mathrm{delay} = 2$ o.c. are also shown in Figs. 1(a)–1(c), respectively. For these three cases, the seventh-frequency laser pulse is added in the rising part, the middle part and the falling part of the fundamental field as shown in Figs. 1(a)–1(c), respectively. Figure 1(d) depicts the harmonic spectra driven by the combined laser field with time delay $t_\mathrm{delay} = -2$ o.c. (the blue

dotted line) and $t_{\rm delay} = 0$ (the green solid line), respectively. We found that there is no spectral shift of the harmonics for $t_{\rm delay} = 0$. However, when the time delay equal to -2 optical cycles, *i.e.*, the seventh-frequency laser pulse is added in the rising part of the fundamental field, the spectral blueshift of the harmonics is observed. Figure 1(e) shows the harmonic spectra for the time delay $t_{\rm delay} = 2$ o.c. (the red dotted line) and $t_{\rm delay} = 0$ (the green solid line), which indicates that the spectral redshift of the harmonics appears for time delay $t_{\rm delay} = 2$ o.c., *i.e.*, the seventh-frequency laser pulse is added in the falling part of the fundamental field.

To investigate the redshift and the blueshift of the harmonics as shown in Figs. 1(d) and 1(e), figures 2(a)–2(c) show the time-frequency analysis of the high-order harmonic spectra with different time delays. In Fig. 2(a), it can be seen that the harmonic efficiency of the falling part is smaller than that of the rising part of the fundamental laser pulse. Therefore, the blueshift is dominant. As shown in Fig. 1(d), the spectral blueshift of the high-order harmonics can be observed when the seventh-frequency laser pulse is added in the rising part of the fundamental field (time delay $t_{\rm delay} = -2$ o.c.). Figure 2(c) shows that the harmonics are dominated by the falling part of the fundamental pulse. Hence for the case of $t_{\rm delay} = 2$ o.c., the harmonics present the spectral redshift (see Fig. 1(e)). In Fig. 2(b), we find that the harmonic emission is symmetrical about $t = 0$ for the case of $t_{\rm delay} = 0$, which presents that no spectral shift of the high-order harmonics appears, as indicated by the green solid line in Figs. 1(d) and 1(e). In addition, we evaluate the harmonic spectrum varying the electric field strength of the seventh-frequency laser field for time delay $t_{\rm delay} = -2$ o.c., and the results are not shown in the text. We find that the harmonic blueshift gradually disappears as the seventh-frequency laser field decreases. We also evaluate the harmonic spectrum varying the electric field strength of the fundamental field for time delay $t_{\rm delay} = 2$ o.c., and the results are not shown in the text. We find that the harmonic emission efficiency in $t < 0$ region gradually is enhanced as the field strength $\boldsymbol{E}_0$ increased. However, the harmonic emission efficiency in $t < 0$ region is still less than that in $t > 0$ region, thus the harmonic spectral shift still appears.

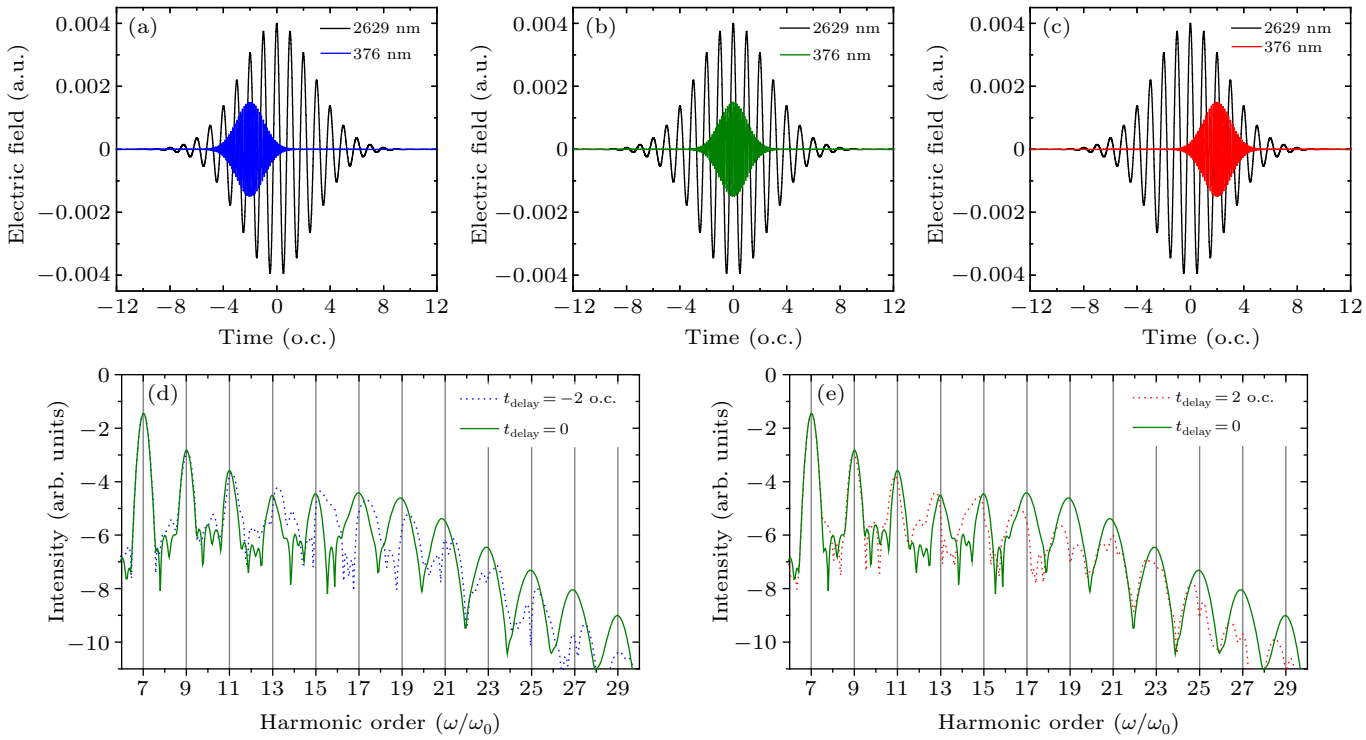


Fig. 1. Electric fields of the 2629-nm fundamental laser pulse (the solid black line) and its seventh-frequency laser pulse with time delay (a) $t_{\rm delay} = -2$ o.c., (b) $t_{\rm delay} = 0$, (c) $t_{\rm delay} = 2$ o.c., respectively. The harmonic spectrum generated by the combined laser fields for different time delays (d) $t_{\rm delay} = -2$ o.c. (the blue dotted line), $t_{\rm delay} = 0$ (the green solid line), and (e) $t_{\rm delay} = 2$ o.c. (the red dotted line), $t_{\rm delay} = 0$ (the green solid line). The field strengths of the fundamental pulse and the seventh-frequency laser pulse are $\boldsymbol{E}_0 = 0.004$ a.u., $\boldsymbol{E}_1 = 0.0015$ a.u., respectively.

Figures 3(a)–3(c) show the harmonic spectra as a function of the crystal momentum $\boldsymbol{k}$ with different time delays. When the time delay equals to -2 optical cycles, the harmonics in the region of around $\boldsymbol{k} = 0$ (the white box) show the spectral blueshift and a clear positive triangle at 11th order harmonic appears as depicted in Fig. 3(a). In contrast, the harmonics generated in the $|\boldsymbol{k}| > 0.13$ a.u. regions (the pink box) as depicted in Fig. 3(a) show the spectral redshift. For the case of $t_{\rm delay} = 2$ o.c., figure 3(c) shows the spectral redshift of the harmonics in the region of around $\boldsymbol{k} = 0$ (the white box), and the harmonics in the $|\boldsymbol{k}| > 0.13$ a.u. regions (the pink box) show the spectral blueshift. In Figs. 3(a) and 3(c), the spectral

shift of the high-order harmonics in the white box is consistent with that illustrated Figs. 1(d) and 1(e). Figure 3(b) shows that there is no spectral shift of the high-order harmonics in the $\boldsymbol{k}$-resolved profile of the harmonics with $t_{\rm delay} = 0$. Moreover, the harmonic intensity minimum can be observed around $\boldsymbol{k} = \pm 0.12$ a.u. as indicated by the black ovals.

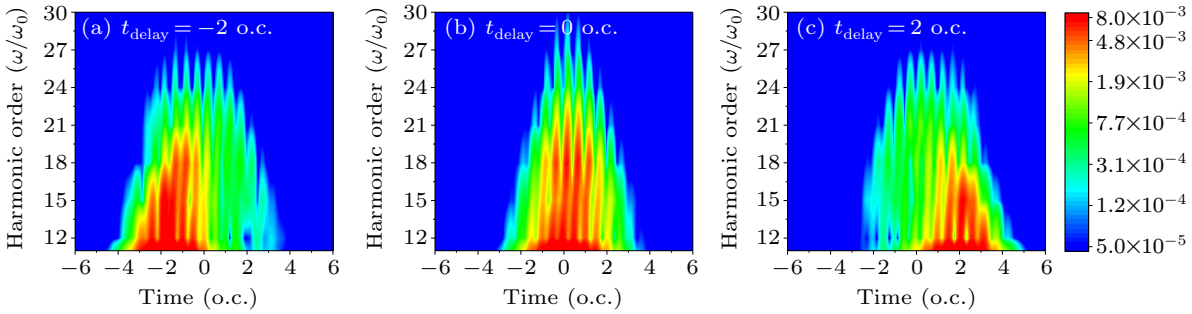


Fig. 2. Time–frequency analysis of the high-order harmonics generated by the combined laser pulses with time delay (a) $t_{\rm delay} = -2$ o.c., (b) $t_{\rm delay} = 0$, and (c) $t_{\rm delay} = 2$ o.c.

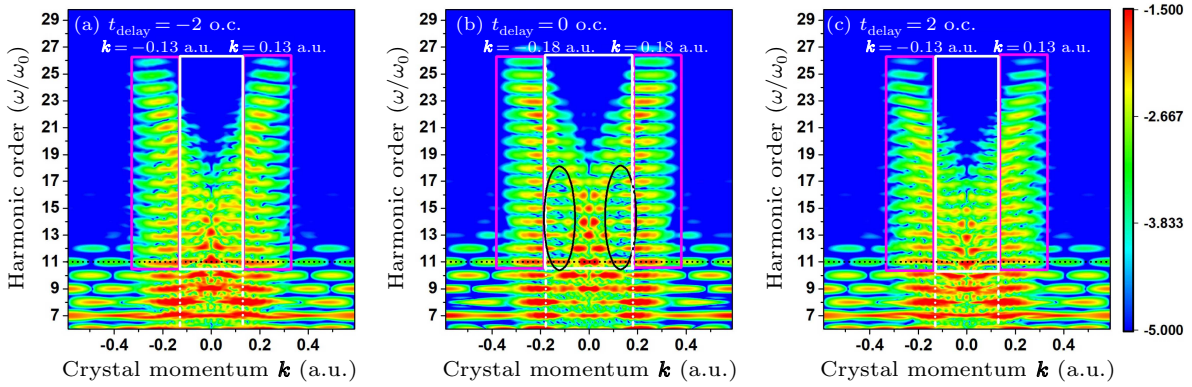


Fig. 3. Crystal-momentum-resolved profile of the harmonic spectra in the combined laser fields with time delay (a) $t_{\rm delay} = -2$ o.c., (b) $t_{\rm delay} = 0$, and (c) $t_{\rm delay} = 2$ o.c.

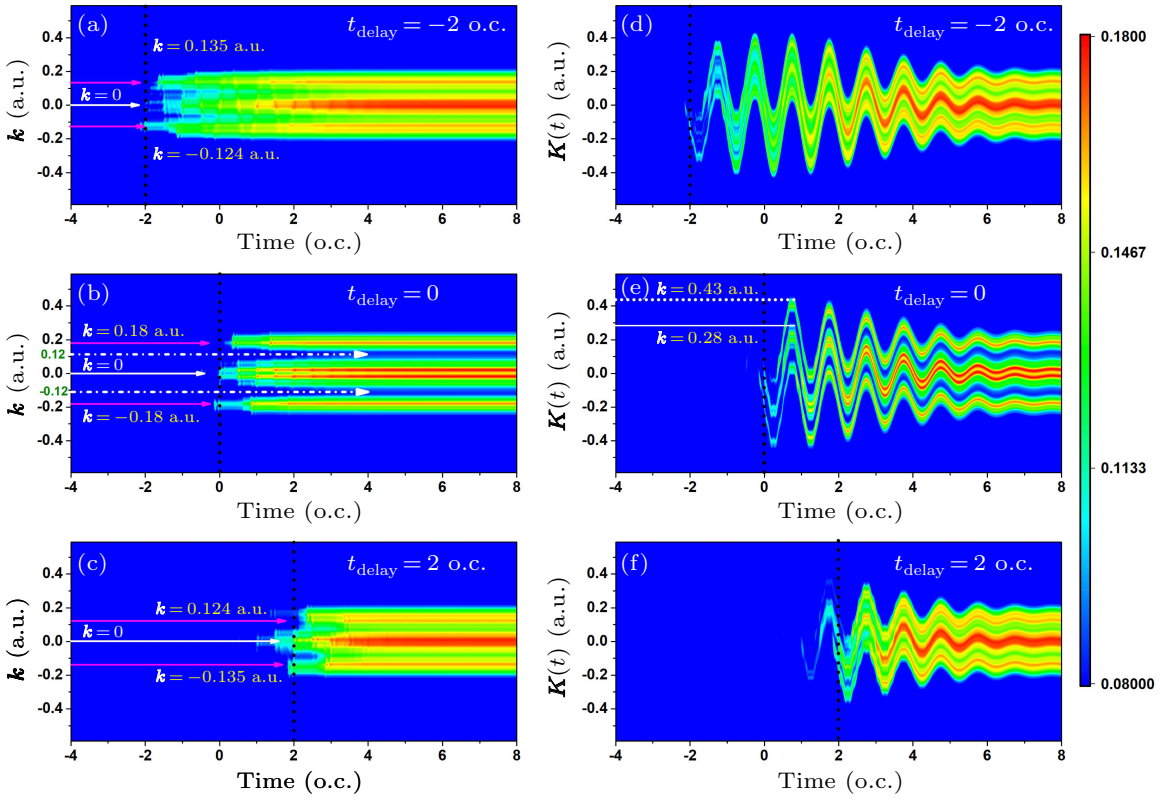


Fig. 4. Time-dependent conduction band population in the initial crystal momentum $\boldsymbol{k}$ space in the combined laser fields with time delay (a) $t_{\rm delay} = -2$ o.c., (b) $t_{\rm delay} = 0$, and (c) $t_{\rm delay} = 2$ o.c. The corresponding time-dependent conduction band population in the moving crystal momentum $\boldsymbol{K}(t)$ space in the combined laser fields with time delay (d) $t_{\rm delay} = -2$ o.c., (e) $t_{\rm delay} = 0$, and (f) $t_{\rm delay} = 2$ o.c.

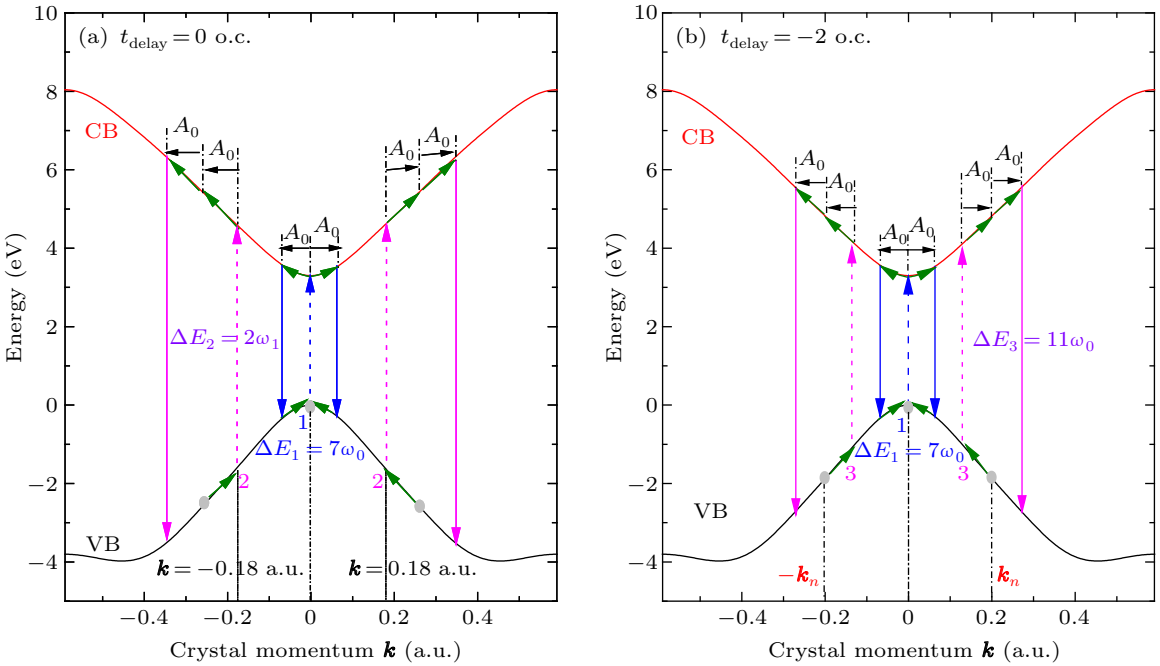


Fig. 5. Energy band structure of the two-band model in reciprocal space. (a) The electrons can be excited to the conduction band via the tunnel ionization channel 1 and the resonant electron injection channels 2 in the combined laser fields with $t_{\rm delay} = 0$. (b) The electrons are promoted via the tunnel ionization channel 1 and the resonant electron injection channels 3 with $t_{\rm delay} = -2$ o.c.

To further illustrate the spectral redshift and blueshift in different crystal momentum as shown in Figs. 3(a)–3(c), we present the time-dependent population in the CB as function of the initial crystal momentum $\boldsymbol{k}$ (in Figs. 4(a)–4(c)) and as a function of the moving crystal momentum $\boldsymbol{K}(t)$ (in Figs. 4(d)–4(e)) with different time delays.[33] And the connection between $\boldsymbol{K}(t)$ and $\boldsymbol{k}$ satisfies $\boldsymbol{K}(t) = \boldsymbol{k} - \boldsymbol{A}(t)$. The black dashed lines in Fig. 4 indicate the position of the maximum amplitude of the seventh-frequency laser pulse. Figure 4(a) presents that the enhanced concentrated electron population appears around $\boldsymbol{k} = 0$ (indicated by the white arrow), and the weak electron population appears around $\boldsymbol{k} = 0.135$ a.u. and $\boldsymbol{k} = -0.124$ a.u. (indicated by the pink arrows) with $t_{\rm delay} = -2$ o.c. For the case of $t_{\rm delay} = 2$ o.c., the weak electron population appears around $\boldsymbol{k} = 0.124$ a.u. and $\boldsymbol{k} = -0.135$ a.u. (indicated by the pink arrows) as shown in Fig. 4(c), and the enhanced concentrated electron population appears around $\boldsymbol{k} = 0$ (indicated by the white arrow). Figure 4(b) presents that the weak electron population appears around $\boldsymbol{k} = \pm 0.18$ a.u. (indicated by the pink arrows) and no electron distribution around $\boldsymbol{k} = \pm 0.12$ a.u. (indicated by the white dashed arrows) with $t_{\rm delay} = 0$, which is caused by the resonant electron injection channels (REIC) as illustrated in Ref. [34]. Therefore, we believe that there are two channels which can excite the electrons around $|\boldsymbol{k}| = 0.135$ a.u., $|\boldsymbol{k}| = 0.124$ a.u. with $t_{\rm delay} = -2$ o.c. or $t_{\rm delay} = 2$ o.c. as shown in Figs. 4(a) and 4(c). Figures 4(d)–4(f) show that the stripe-like distribution appears in the time-dependent conduction band population in the $\boldsymbol{K}(t)$ space by adding the seventh-frequency laser pulse to the fundamental laser pulse, which is also due to the generation of the channels.

A clear physical picture can help us understand the channels in $\boldsymbol{k}$ space for different time delays. Figure 5 shows the energy band structure of the two-band model in reciprocal space for time delay $t_{\rm delay} = 0$ and $t_{\rm delay} = -2$ o.c. It is shown that the electrons can be excited to the CB via two channels, respectively. And the channel 1 (the blue dashed arrow as shown in Figs. 5(a) and 5(b)) is the tunneling ionization channel, which occurs only at the top of the VB and need absorb $7\omega_0$ photons. The oscillations of the electrons driven by the laser field in the VB and CB need to satisfy the Bloch acceleration theorem $\boldsymbol{K}(t) = \boldsymbol{k} - \boldsymbol{A}(t) = \boldsymbol{k} + \frac{e}{\hbar}\int_{t_0}^{t} \boldsymbol{E}(t')\,{\rm d}t'$, where $\boldsymbol{k} = \boldsymbol{K}(t_0)$ is the initial crystal momentum.[35,36] The solid white line in Fig. 4(e) indicates the maximum momentum $\boldsymbol{K}(t) = 0.28$ a.u. that the electron can acquire after being excited to the conduction band through the channel 1. According to $\boldsymbol{K}(t) = \boldsymbol{k} + \boldsymbol{A}_0$, we obtain that $\boldsymbol{k} = 0.05$ a.u. Thus the electrons at $\boldsymbol{k} = 0.05$ a.u. in the VB can reach the position of channel 1 through the pre-acceleration process[37] (the green arrows as shown in Figs. 5(a) and 5(b)) and then be injected into the CB via channel 1 (the blue dashed arrow). The electrons excited by the channel 1 oscillate periodically in the CB (the solid green arrows) and are restricted in $\boldsymbol{k} \in [-\boldsymbol{A}_0, \boldsymbol{A}_0]$ as indicated in Fig. 5. As the laser field is inverted, the electron and the hole recombine and generate the high-order harmonics (the solid blue arrows).

Figure 5(a) shows that the electrons in the VB also can be excited to CB through the resonant electron injection channels 2 (the pink dashed arrows) at $\boldsymbol{k} = \pm 0.18$ a.u. and need absorb $2\omega_1$ photons with $t_{\rm delay} = 0$ as illustrated in Ref. [34]. The

dashed white line in Fig. 4(e) indicates the maximum momentum $\boldsymbol{K}(t) = 0.43$ a.u. that the electron can acquire after being excited to the conduction band through the channel 2. According to $\boldsymbol{K}(t) = \boldsymbol{k} + \boldsymbol{A}_0$, we obtain that $\boldsymbol{k} = 0.2$ a.u. Thus the electrons near $\boldsymbol{k} = \pm 0.18$ a.u. in the VB can reach the channel 2 by the pre-acceleration (the green arrows in Fig. 5(a)) and then be excited to the CB via channel 2. The generation of the channels 2 leads to the minimum of the harmonic intensity around $\boldsymbol{k} = \pm 0.12$ a.u. as indicated by the black ovals in Fig. 3(b). For the case of $t_{\text{delay}} = -2$ o.c., figure 5(b) shows that the electrons can be excited to the CB through the tunnel ionization channel 1 (the blue dashed arrow) and channels 3 (the pink dashed arrows). Channels 3 is also the resonant electron injection channels, which will be illustrated in the following discussion. The energy difference between the CB and VB of the channels 3 corresponds to $11\omega_0$ photons. For the electron at the initial momentum $\boldsymbol{k}_n$ in the VB as indicated in Fig. 5(b), the electron in the VB can reach the position of channels 3 through the preacceleration process (the green solid arrow) and can be excited to the CB (the pink dashed arrow). The electrons oscillate periodically in the $\boldsymbol{k} \in [\boldsymbol{k}_n - \boldsymbol{A}_0, \boldsymbol{k}_n + \boldsymbol{A}_0]$ region (the green solid arrows) in the CB, and then combined with hole in the VB to generate the high-order harmonics (the pink solid arrow).

Figures 6(a)–6(c) show the time-dependent population of CB in $\boldsymbol{k}$ space generated by the combined fields for $\boldsymbol{E}_0 = 0.004$ a.u., $\boldsymbol{E}_1 = 0.0015$ a.u. with different time delays. We found that, as the time delays increase, the position of the channels (the pink arrow) gradually approach to $\boldsymbol{k} = 0$. Therefore, the position of the channels is related to the time delay of the two laser pulses. Thus we can also call the channel 3 the REIC as illustrated in Ref. [34]. Figures 6(d)–6(f) show the time-dependent population of CB in $\boldsymbol{k}$ space generated by the combined fields for $t_{\text{delay}} = -2$ o.c., $\boldsymbol{E}_0 = 0.004$ a.u. with different strengths of the seventh-frequency laser pulses. It is shown that, as the intensity of the seventh-frequency laser pulse increases, the position of the channels 3 remains unchanged but the population gradually increase (as indicated by the pink arrow), which means that the contribution of the electrons from channels 3 to the harmonics depends on the seventh-frequency laser pulse. The energy difference between the CB and VB of the channels 3 corresponds to $11\omega_0$ photons as indicated in Fig. 5(b), thus we can also think that the electrons from channels 3 absorb ω_1 photon and $4\omega_0$ photons (*i.e.*, $11\omega_0 = \omega_1 + 4\omega_0$) and then be excited to the CB.

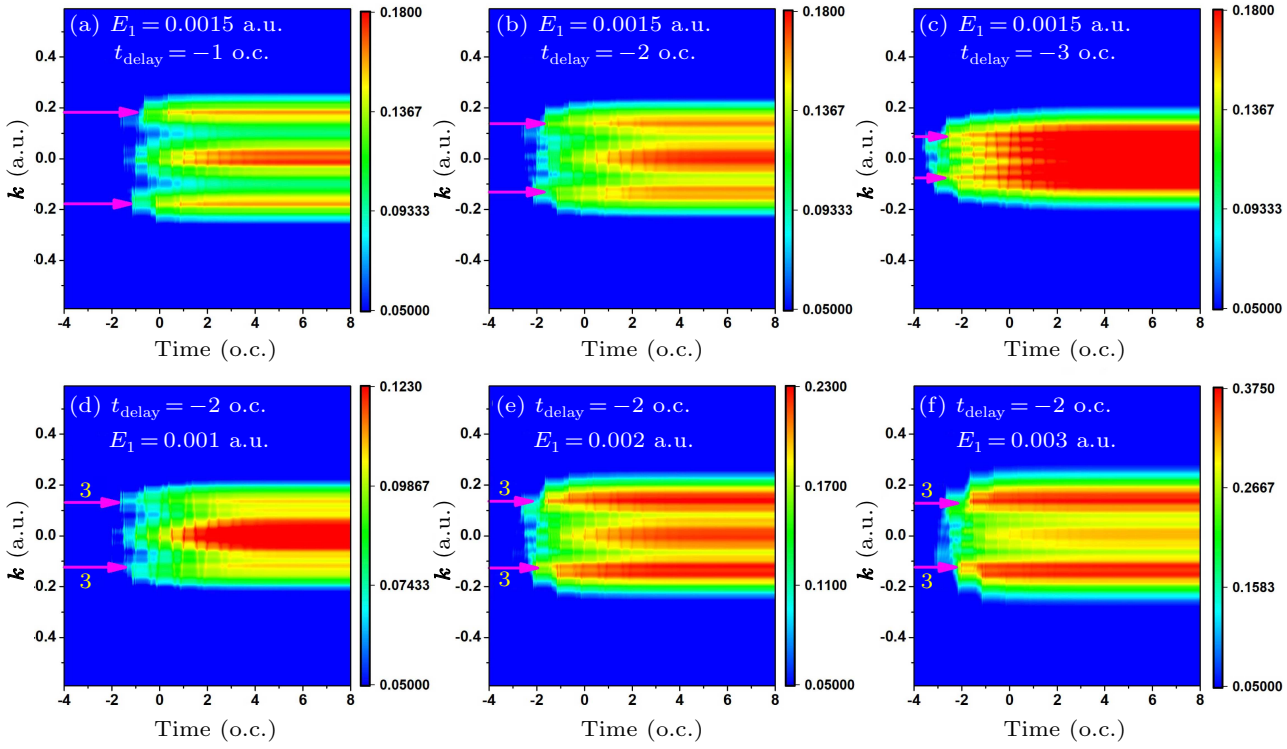


Fig. 6. Time-dependent population of CB in $\boldsymbol{k}$ space generated by the combined fields for $\boldsymbol{E}_0 = 0.004$ a.u., $\boldsymbol{E}_1 = 0.0015$ a.u. with time delay (a) $t_{\text{delay}} = -1$ o.c., (b) $t_{\text{delay}} = -2$ o.c., and (c) $t_{\text{delay}} = -3$ o.c. Time-dependent population of CB in $\boldsymbol{k}$ space generated by the combined fields for $\boldsymbol{E}_0 = 0.004$ a.u., $t_{\text{delay}} = -2$ o.c. with different strengths of the seventh-frequency laser pulses (d) $\boldsymbol{E}_1 = 0.001$ a.u., (e) $\boldsymbol{E}_1 = 0.002$ a.u., and (f) $\boldsymbol{E}_1 = 0.003$ a.u.

To better illustrate the spectral blueshift and the spectral redshift of the harmonics from the channel 1 (the white box) and the channel 3 (the pink box) as shown in Figs. 3(a) and 3(c), we define the region of $\boldsymbol{k} \in (-0.1$ a.u.$, 0.1$ a.u.$)$ in the VB as Ω_1 (the blue arrow) and the region of $\boldsymbol{k} \in (-0.3$ a.u.$, -0.1$ a.u.$)$ as Ω_2 (the red arrow) as shown in Fig. 7(a). And region Ω_1 and region Ω_2 correspond to the electrons be excited through the channel 1 and the channel 3, respectively. Figures 7(b) and 7(c) show the $\boldsymbol{k}$-integrated transient CB population of the electrons from region Ω_1 (the blue

solid line) and region Ω_2 (the red solid line) with time delay $t_{\rm delay} = -2$ o.c. and $t_{\rm delay} = 2$ o.c., respectively. To show more clearly the excitation process of electrons from region Ω_1 and region Ω_2, the insets in the lower right corner of Figs. 7(b) and 7(c) give the details. For the case of $t_{\rm delay} = -2$ o.c., the electron population in region Ω_2 at $t = -2$ o.c. is enhanced as indicated by the green dashed line. However, the electron population in region Ω_1 at $t = -2.5$ o.c. is enhanced as indicated by the green dashed line. In addition, the inset of Fig. 7(b) shows that almost all the electrons from region Ω_1 are excited to the CB at $t = 3.4$ o.c., and the CB population almost remains unchanged after $t = 3.4$ o.c. For region Ω_2, the electrons are not almost all excited to the CB until $t = 3.9$ o.c. Thus there is a certain delay in the excitation process of the electrons from region Ω_2 compared with that from region Ω_1 (as indicated by the black arrow in the inset of Fig. 7(b)). The delayed population will lead to the delay of the harmonic emission process,[24,29] and this will result in the spectral redshift of the harmonics (as shown in the pink box of Fig. 3(a)). The excited process of the electrons from region Ω_1 is lie in the smallest band gap, the electrons from region Ω_1 makes the main contribution to the harmonic spectrum. Thus the harmonics generated by the electrons from region Ω_1 (the white box as shown in Fig. 3(a)) and the harmonics as shown in the blue dotted line in Fig. 1(d) both show the spectral blueshift.

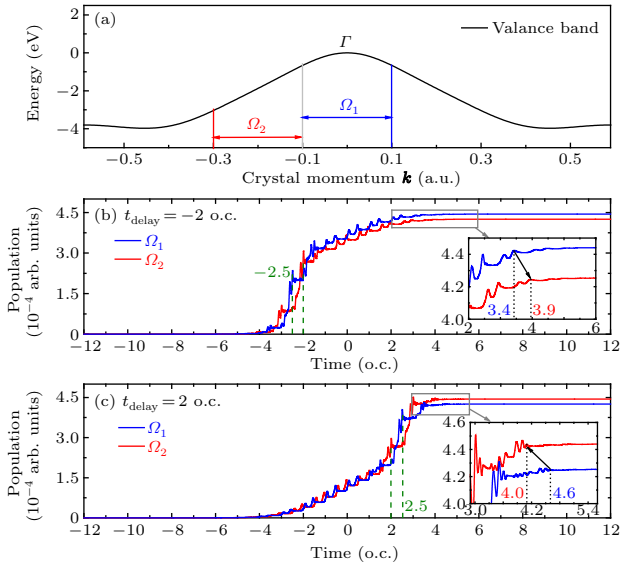


Fig. 7. (a) The sectionalization of crystal momentum for the electrons in valence band. The Ω_1 and Ω_2 correspond to the crystal momentum intervals of $[-0.1$ a.u.$, 0.1$ a.u.$]$ and $[-0.3$ a.u.$, -0.1$ a.u.$]$, respectively. The $\boldsymbol{k}$-integrated transient CB population generated by the electrons within Ω_1 (the blue solid line) and Ω_2 (the red solid line) in the combined laser fields at $\boldsymbol{E}_1 = 0.0015$ a.u. with time delay (b) $t_{\rm delay} = -2$ o.c. and (c) $t_{\rm delay} = 2$ o.c.

For the case of $t_{\rm delay} = 2$ o.c., the electron population in region Ω_2 at $t = 2$ o.c. is enhanced as indicated by the green dashed line. However, the electron population in region Ω_1 at $t = 2.5$ o.c. is enhanced as indicated by the green dashed line. And the inset of Fig. 7(c) indicates that almost all the electrons from region Ω_2 are excited to the CB at $t = 4.0$ o.c. However, the electrons from region Ω_1 are not completely excited to the CB until $t = 4.6$ o.c. Compared with region Ω_1, the electrons from region Ω_2 are excited to the CB earlier (as indicted by the black arrow in the inset of Fig. 7(c)), which results in the spectral blueshift of the harmonics (as shown in the pink box of Fig. 3(c)). The harmonics generated by the electrons from region Ω_1 (the white box as shown in Fig. 3(c)) and the harmonics shown by the red dotted line in Fig. 1(e) both show the spectral redshift.

4. Conclusion

In summary, we have investigated the high-order harmonic spectral shift of the one-dimensional ZnO crystal in a combined laser field by solving the semiconductor Bloch equations, and the combined laser field is synthesized by a fundamental laser pulse and its seventh-frequency laser pulse. Through time-frequency analysis, we find that the spectral shift is caused by the unequal contribution of the rising and falling parts of the laser field to the harmonics. By analyzing the time-dependent conduction band population in $\boldsymbol{k}$ space, we found that the REIC is induced by the seventh-frequency laser pulse. And the position of the REIC can be controlled by changing the time delay of the two laser pulses. When the seventh-frequency laser pulse is added to the rising part of the fundamental laser field, the harmonics generated by the tunneling ionization channel and REIC show the spectral blueshift and the spectral redshift, respectively. By analyzing the $\boldsymbol{k}$-integrated transient CB population of the two channels, we found that it is the inconsistent electrons excitation times of the two channels leading to the harmonics of the two channels show spectral blueshift and spectral redshift, respectively.

Acknowledgment

Project supported by the National Natural Science Foundation of China (Grant Nos. 12074142 and 11904122).

References

[1] Krausz F and Ivanov M 2009 *Rev. Mod. Phys.* **81** 163
[2] Mourou G A, Labaune C L, Dunne M, Naumova N and Tikhonchuk V T 2007 *Plasma Phys. Contr. Fusion* **49** B667
[3] Lewenstein M, Balcou Ph, Ivanov M Y, L'Huillier A and Corkum P B 1994 *Phys. Rev. A* **49** 2117
[4] Wang X W, Wang L, Xiao F, Zhang D W, Lü Z H, Yuan J M and Zhao Z X 2020 *Chin. Phys. Lett.* **37** 023201
[5] Zhang H D, Liu X W, Jin F C, Zhu M, Yang S D, Dong W H, Song X H and Yang W F 2021 *Chin. Phys. Lett.* **38** 063201
[6] Paul P M, Toma E S, Breger P, Mullot G, Augé F, Balcou Ph, Muller H G and Agostini P 2001 *Science* **292** 1689
[7] Xia C L, Zhang G T, Wu J and Liu X S 2010 *Phys. Rev. A* **81** 043420
[8] Zhang J, Qi T, Pan X F, Guo J, Zhu K G and Liu X S 2019 *Chin. Phys. B* **28** 103204
[9] Guan Z, Wang G L, Zhang L, Jiao Z H, Zhao S F and Zhou X X 2021 *Chin. Phys. Lett.* **38** 054201
[10] Zhu Y P, Liu Y R, Zhao X, Kimberg V and Zhang S B 2021 *Chin. Phys. Lett.* **38** 053201

[11] Itatani J, Levesque J, Zeidler D, Niikura H, Pépin H, Kieffer J C, Corkum P B and Villeneuve D M 2004 *Nature* **432** 867
[12] Ghimire S, DiChiara A D, Sistrunk E, Agostini P, DiMauro L F and Reis D A 2011 *Nat. Phys.* **7** 138
[13] Vampa G, Hammond T J, Thiré N, Schmidt B E, Légaré F, McDonald C R, Brabec T and Corkum P B 2015 *Nature* **522** 462
[14] Vampa G, McDonald C R, Orlando G, Klug D D, Corkum P B and Brabec T 2014 *Phys. Rev. Lett.* **113** 073901
[15] Vampa G, McDonald C R, Orlando G, Corkum P B and Brabec T 2015 *Phys. Rev. B* **91** 064302
[16] Liu X, Li L, Zhu X S, Huang T F, Zhang X F, Wang D, Lan P F and Lu P X 2018 *Phys. Rev. A* **98** 063419
[17] He Y L, Guo J, Gao F Y, Yang Z J, Zhang S Q and Liu X S 2021 *Phys. Rev. A* **104** 013104
[18] Wu M X, Browne D A, Schafer K J and Gaarde M B 2016 *Phys. Rev. A* **94** 063403
[19] Guan Z, Zhou X X and Bian X B 2016 *Phys. Rev. A* **93** 033852
[20] Fu S L, Feng Y K, Li J B, Yue S J, Zhang X, Hu B T and Du H C 2020 *Phys. Rev. A* **101** 023402
[21] Hansen K K, Deffge T and Bauer D 2017 *Phys. Rev. A* **96** 053418
[22] Du H C, Xue S, Wang H Q, Zhang Z L and Hu B T 2015 *Phys. Rev. A* **91** 063844
[23] Zhang J, Pan X F, Xu T T and Liu X S 2017 *Laser Phys. Lett.* **14** 055302
[24] Pan X F, Li B, Han T, Zhang J and Liu X S 2020 *Laser Phys.* **30** 035301
[25] Shin H J, Lee D G, Cha Y H, Hong K H and Nam C H 1999 *Phys. Rev. Lett.* **83** 2544
[26] Hädrich S, Rothhardt J, Krebs M, Tavella F, Willner A, Limpert J and Tünnermann A 2010 *Opt. Express* **18** 20242
[27] Kan C, Capjack C E, Rankin R and Burnett N H 1995 *Phys. Rev. A* **52** R4336
[28] Watson J B, Sanpera A and Burnett K 1995 *Phys. Rev. A* **51** 1458
[29] Jia G R, Huang X H and Bian X B 2017 *Opt. Express* **25** 23654
[30] Navarrete F, Ciappina M F and Thumm U 2019 *Phys. Rev. A* **100** 033405
[31] Bloch F 1929 *Z. Phys.* **52** 555
[32] McDonald C R, Vampa G, Corkum P B and Brabec T 2015 *Phys. Rev. A* **92** 033845
[33] Song X H, Yang S D, Zuo R X, Meier T and Yang W F 2020 *Phys. Rev. A* **101** 033410
[34] Sun N, Zhu X S, Li L, Lan P F and Lu P X 2021 *Phys. Rev. A* **103** 053111
[35] Du T Y and Bian X B 2017 *Opt. Express* **25** 151
[36] Song X H, Zuo R X, Yang S D, Li P C, Meier T and Yang W F 2019 *Opt. Express* **27** 2225
[37] Li L, Lan P F, Zhu X S, Huang T F, Zhang Q B, Lein M and Lu P X 2019 *Phys. Rev. Lett.* **122** 193901